Nuclear Mapping of Nanodrug Delivery Systems in Dynamic Cellular Environments

Ashwinkumar A. Bhirde,[†] Ankur Kapoor,[‡] Gang Liu,[§] Ramiro Iglesias-Bartolome,[⊥] Albert Jin,[∥] Guofeng Zhang,[∥] Ruijun Xing,[†] Seulki Lee,[†] Richard D. Leapman,[∥] J Silvio Gutkind,[⊥] and Xiaoyuan Chen[†,*]

[†]Laboratory of Molecular Imaging and Nanomedicine, National Institute of Biomedical Imaging and Bioengineering, National Institutes of Health, Bethesda, Maryland 20892, United States, [‡]Department of Radiology and Imaging Sciences, Clinical Center, National Institutes of Health, Bethesda, Maryland 20892, United States, [§]Center for Molecular Imaging and Translational Medicine, School of Public Health, Xiamen University, Xiamen 361005, China, [⊥]Oral and Pharyngeal Cancer Branch, National Institute of Dental and Craniofacial Research, National Institutes of Health, Bethesda, Maryland 20892, United States, and [∥]Laboratory of Cellular Imaging and Macromolecular Biophysics, National Institute of Biomedical Imaging and Bioengineering, National Institutes of Health, Bethesda, Maryland 20982, United States

ABSTRACT

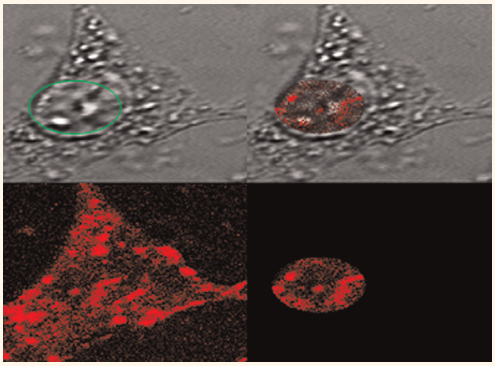

Nanoformulations have shown great promise for delivering chemotherapeutics and hold tremendous clinical relevance. However nuclear mapping of the chemodrugs is important to predict the success of the nanoformulation. In this study fluorescence microscopy and a subcellular tracking algorithm were used to map the diffusion of chemotherapeutic drugs in cancer cells. Positively charged nanoparticles efficiently carried the chemodrug across the cell membrane. The algorithm helped map free drug and drug-loaded nanoparticles, revealing a varying nuclear diffusion pattern of the chemotherapeutics in drug-sensitive and -resistant cells in a live dynamic cellular environment. While the drug-sensitive cells showed an exponential uptake of the drug with time, resistant cells showed random and asymmetric drug distribution. Moreover nanoparticles carrying the drug remained in the perinuclear region, while the drug accumulated in the cell nuclei. The tracking approach has enabled us to predict the therapeutic success of different nanoscale formulations of doxorubicin.

KEYWORDS: iron oxide nanoparticles · doxorubicin · drug resistance · computational · nuclear mapping · live cell imaging · cancer

Although a number of chemotherapeutic drugs are available to treat various cancers, severe toxicity and unpredictable efficacy are frequently seen with existing therapies.[1,2] In addition, significant limitations exist with chemotherapy, including inadequate dosing at the disease sites, acute and long-term drug toxicity, and possible tumor recurrence as a result of drug resistance.[3−7] To counteract these difficulties, combinations of chemotherapeutic drugs and nanomaterials[8] have been formulated to deliver drugs at high concentrations to the sites of disease while maintaining lower and less toxic systemic concentrations in the patient. Various organic/inorganic, biological, and synthetic nanomaterials are currently under investigation for these nanodrug formulations.[9−15] Enzyme- and pH-responsive and receptor-specific nanodrug formulations are major ones being developed.[16] Among the imaging modalities, PET, CT, and MRI have been the most widely used and clinically implemented techniques. For molecular and functional imaging strategies used in nanodrug development, bioluminescence and fluorescence imaging have evolved as important imaging tools.[17]

Chemotherapeutic drugs, *e.g.*, cisplatin and doxorubicin, kill cancer cells by intercalating with the DNA, thereby disrupting the cell growth and division process.[18−20] However, even with advanced nanodrug formulations, the delivery of an insufficient drug concentration to the nuclei of tumor cells in the patient may lead to unsuccessful treatment.[21] Use of live cell fluorescence microscopy for imaging the subcellular distributions of drugs is critical for assessing the biological effects of chemotherapeutic formulations.[22] Recent advances in live cell imaging have included the ability to track cells automatically.[23] However, most algorithms for cellular tracking require the use of fluorescent signals originating from genetically modified proteins.[24] Here, we have developed a technique for directly tracking chemotherapeutics successfully in single cells based on the intrinsic fluorescence of the drug without using selective stains or fluorescent proteins as labels.

* Address correspondence to shawn.chen@nih.gov.

Received for review February 4, 2012 and accepted April 27, 2012.

Published online April 27, 2012
10.1021/nn300516g

The nanodrug formulation that we have constructed combines the drug doxorubicin (DOX) and superparamagnetic iron oxide nanoparticles (SPIONPs). Magnetic nanocrystals like SPIONPs have been developed mainly as MRI contrast agents and as magnetic labels for tracking stem cells.[25−27] DOX is an FDA-approved drug, which is a clinically relevant chemotherapeutic for a variety of cancers, particularly ovarian cancer.[28,29] It has been demonstrated that SPIONPs can function as drug delivery vehicles to reach tumor sites and can also be imaged through MR contrast.[30−33] Although the loading of SPIONPs with chemotherapeutic drugs has recently been investigated,[34,35] there are no reports of live imaging of the entire drug delivery system, including the drug itself in a dynamic cellular environment. We have synthesized highly aqueous, dispersed polyethyleneimine (PEI)-coated SPIONPs[36] and loaded them with doxorubicin. Our aim is to test the efficacy of the nanoparticles against drug-sensitive and drug-resistant cancer cells, as well as to characterize subcellular differences in translocation and accumulation between the free drug and the nanodrug delivery system.

RESULTS AND DISCUSSION

Synthesis and Characterization of Nanodrug Delivery System. The nanodrug formulation was formed by first synthesizing SPIONP nanocrystals using branched PEI2k. DOX was loaded onto the magnetic nanocrystals, and the entire drug delivery system was thoroughly characterized for size, shape, surface charge, and drug loading efficiency (Figure 1 and Supporting Information Figures S1−S3). The as-synthesized highly aqueous dispersed PEI-coated magnetic nanocrystals were characterized with a transmission electron microscope (Figure 1a) and an atomic force microscope (Figure 1b), which showed a core size of ∼10−15 nm and a overall size of ∼50−60 nm, respectively. PEI coating onto the SPIONPs was confirmed by FTIR and zeta-potential analysis. The FTIR spectrum (Supporting Information Figure S1) showed the presence of amine groups on the magnetic nanoparticles at around 1400−1700 nm wavelength. A surface charge of 44.3 mV of the SPIONPs confirms efficient coating of the charged polymer. Fluorescence spectroscopy (Supporting Information Figure S2) confirmed the presence of doxorubicin on the SPIONPs. DOX loading onto the nanoparticles was done using fluorescence analysis on a microplate reader (Supporting Information Figure S3). The Nanodox was treated with diluted HCl (pH = 5) and incubated for 20 min. The DOX content was quantified at 590 nm on the microplate reader by comparing with a standard curve.

Computational Nuclear Mapping Modeling. Whereas nuclear boundaries are often clearly demarcated in microscopy of fixed cells, in live cell microscopy the boundaries are often not well defined due to the dynamically changing morphology. Furthermore, since the cells are not fixed, they may migrate away from the focal plane of the image. To take these factors into account, we have developed a semiautomated method for tracking cell nuclei in a recorded time sequence of live images. The first step in the process, shown as a flow diagram in Figure 2a, allows the user to pick an elliptical region that defines the nuclear boundary in the first image of a recorded time series. This region is used as a template to match the nucleus in subsequent images. To provide a similarity measure between the template (T) and image (I), a normalized cross correlation (NCC) function is defined according to

$$\mathrm{NCC}(u,v) = \frac{\sum_{u,v}(I(x,y) - \overline{I_{u,v}})(T(x,y) - \bar{T})}{\sigma_I \sigma_T}$$

where $\bar{T}$ and $\bar{I}\,u,v$ are mean values of the template and an image region under the template, respectively, and σ_T and σ_I are the corresponding standard deviations.

The location (u,v) in the image that maximizes NCC is considered to be the location of the elliptical region that best matched the current template. Additionally, a new elliptical region around this location replaces the current template, which is then used for the next

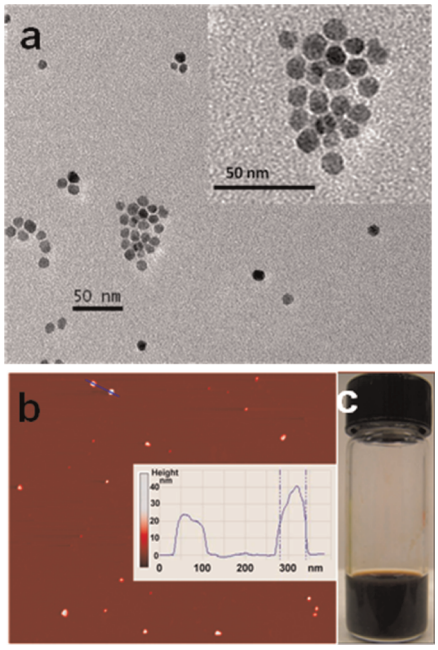

Figure 1. Electron and force microscopy characterization of nanodrug delivery vehicles. (a) Transmission electron microscope (TEM) characterization of Alkyl-PEI2k-SPIONPs. TEM was used to characterize the shape and size of the material core. TEM analysis showed 10−15 nm spherical magnetic nanocyrstals. (b) Atomic force microscope (AFM) and surface charge analysis of the Alkyl-PEI2k-SPIONPs. AFM characterization gave the hydrodynamic size of the NPs, which was greater than 15 nm and less spherical than observed from TEM, confirming the polymer coating. (c) Picture showing highly aqueous dispersed iron oxide nanoparticles with zeta-potential analysis showing a high positive charge of 44.3 mV on the nanoparticles.

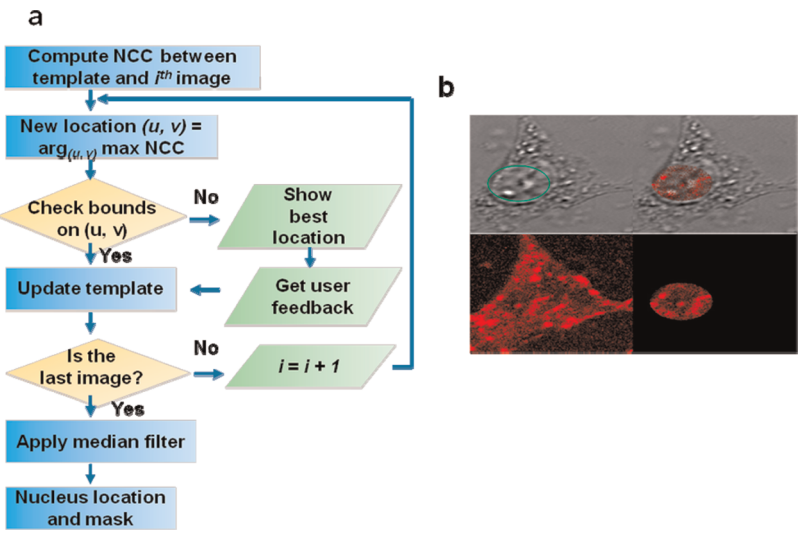

Figure 2. Flowchart for computational nucleus tracking and representative nuclear mapping of DOX in a dynamic cellular environment in cancer cells. (a) The flowchart for tracking and mapping in live microscopy images shows the outline of the algorithm to obtain the location and mask of the nucleus in live imaging. The location and mask are updated for each new time point in the live image and used to compute the drug accumulation using the corresponding fluorescent channels. (b) Screen capture of the output of the algorithm, where the top left image shows the superposition of the nucleus boundary on the optical image at a given time point. The bottom left shows the corresponding DOX channel at the same time point. The bottom right shows the DOX channel intensity after applying the nucleus location and mask computed by the algorithm. After application of this mask, the image shows only intensity that is contained inside the nucleus. Since location and mask are updated continuously, the fluorescent channel intensity shown corresponds to the location of the nucleus in the current image. The top right image is the fusion of optical image and the bottom right image.

image. This process is repeated until all the images in the time series are analyzed. A log of locations of centers of elliptical regions is maintained for each of these images.

There is a possibility that NCC may not result in a correct match due to noise and ill-defined nucleus boundaries. To mitigate this scenario, we place bounds on the allowed displacement in the centers of elliptical regions between two consecutive images. The allowed displacement is determined heuristically based on the size of the elliptical region and the size of the image. If maximization of NCC fails to find a new location, the algorithm stops for a user input. A probable location based on past cell motion is presented to the user, who can adjust this location manually using a graphical user interface. The algorithm resumes by using this manually updated location for the next iteration of the NCC-based algorithm (Supporting Information Note). Once the entire series is processed, a median filter of 5 pixel width is applied to smooth the trajectory of the elliptical region center. Finally, this elliptical region with a smooth trajectory is used as a mask to compute the distribution of drug or drug-loaded nanoparticles inside the nucleus. A simple representative snapshot of the result of the algorithm is shown in Figure 1b, where the top panel shows optical tracking of a whole cell with marked nuclei, while the bottom panel shows the fluorescent view of the whole cell and nucleus alone in a single cancer cell.

Nuclear Mapping of Nano-chemotherapeutics in Drug-Sensitive Cells. Our study involved two drug delivery systems studied in drug-sensitive and drug-resistant cells: the FDA approved DOX drug adramycin and DOX-loaded SPIONPs (Nanodox). These were both tested for cell penetration and nuclear accumulation. DOX-sensitive OVCAR8 cancer cells were treated with either free drug or Nanodox (Supporting Information Videos S1, S2). Live microcopy monitoring showed the presence of the drug in the cells as early as 25 min for the free drug and 5 min for the Nanodox (Figure 3a and Supporting Information Videos S3, S4). Cells treated with free drug and Nanodox formulation and showing DOX accumulation were also fixed and stained for organelle localization (Figure 1c) 1 h post-treatment. Analysis of Z-stack images of the fixed cells showed nuclear drug uptake in drug-sensitive cells from both free drug and Nanodox. However, nuclear mapping using our tracking algorithm showed a marked difference between early uptake of the free drug and uptake of the drug loaded onto the SPIONPs (Figure 1d). The overall cellular uptake of the Nanodox was 5-fold higher than the drug on its own in 60 min (Figure 1e). After washing and incubation with medium for 3 h, the presence of DOX was clearly observed in the nuclear region for both free drug and Nanodox (Supporting Information Figure S4). The uptake of drug into the drug-sensitive cells was exponential in both nuclear and non-nuclear cellular regions. Notably the Nanodox formulation was able to take a minimal dosage to the cancer cell nuclei in the concentrated amount that is clinically desired.

Nuclear Mapping of Nano-chemotherapeutics in Drug-Resistant Cells. Drug-resistant OVCAR8/ADR cancer cells

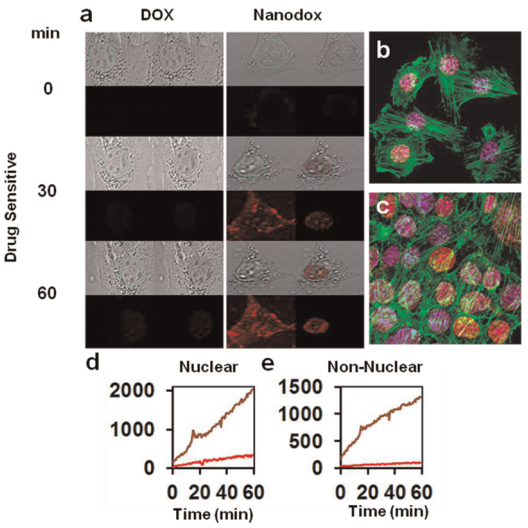

Figure 3. Representative nuclear mapping of DOX in a dynamic cellular environment. (a) OVCAR8 (drug-sensitive) cells treated with free drug and Nanodox at 0, 30, and 60 min. (b) Fixed cell images of drug-sensitive cells treated with free drug and Nanodox and fixed post 1 h treatment. Cell nuclei are stained in blue and actin is stained in green, while the drug is in red. Both free drug and Nanodox show nuclear accumulation. Free drug shows hardly any drug accumulation, and Nanodox shows nuclear accumulation to some extent. (d, e) Plot showing nuclear and non-nuclear intensity of DOX with time in drug-sensitive cancer cells. Exponential uptake pattern is observed with both free drug and Nanodox in drug-sensitive cells. Nanodox shows significantly higher drug uptake than free DOX ($p < 0.01$). Most importantly nuclear accumulation of DOX is higher compared to non-nuclear regions for Nanodox.

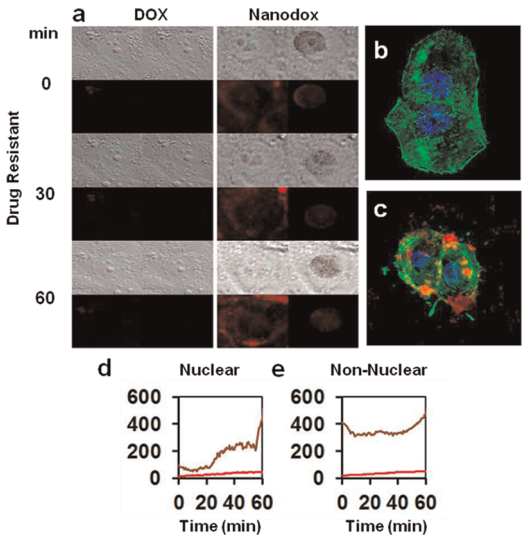

Figure 4. (a) Nuclear mapping of DOX in resistant cancer cells in a dynamic cellular environment and OVCAR8/ADR (drug-resistant) cells treated with free drug and Nanodox at 0, 30, and 60 min. (b, c) Fixed cell images of drug-resistant cells treated with free drug and Nanodox and fixed post 1 h treatment. Cell nuclei are stained in blue and actin stained in green, while the drug is in red. Both free drug and Nanodox show nuclear accumulation. Free drug shows hardly any drug accumulation, and Nanodox shows nuclear accumulation to some extent. (d, e) Plots showing nuclear and non-nuclear intensity of DOX with time in the drug-sensitive cancer cells (d) and in the drug-resistant cancer cells (e). Drug uptake pattern in the drug-resistant cells is entirely different from that in the drug-sensitive cells for both free DOX and Nanodox. Nanodox shows a sudden burst of drug uptake in the nuclear region after 30 min, while there is no appreciable free drug uptake in the cell nuclei.

were treated with free DOX and Nanodox and observed live in a dynamic environment (Supporting Information Videos S5, S6). Nuclear mapping with the drug-resistant OVCAR8/ADR cells showed a sharp contrast between the uptake of the free drug and uptake of the drug loaded onto SPIONPs (Figure 4a and Supporting Information Videos S7, S8). The overall cellular uptake of the Nanodox was almost 5 times greater than the drug on its own at the 60 min time point. The free drug and Nanodox had similar uptake profiles for the first 30 min of treatment in the resistant cells. This behavior was quite different from that of drug-sensitive cells. After incubation with medium for 3 h, the presence of drug was still observed in 90% of the Nanodox-treated cells, but was rarely seen in free DOX-treated cells, as the free drug was readily effluxed from the drug-resistant cells (Supporting Information Figure S5). Uptake of free DOX on its own was observed only in a couple of cells, which crossed the cell membrane and reached the cell nucleus. Nanodox was the most effective in crossing the cellular barrier. DOX on the SPIONPs was able to penetrate almost all the DOX-resistant cancer cells, with a couple of cells showing nuclear uptake. Data obtained show very high cellular penetration of the nanoformulation, which can counteract drug resistance.

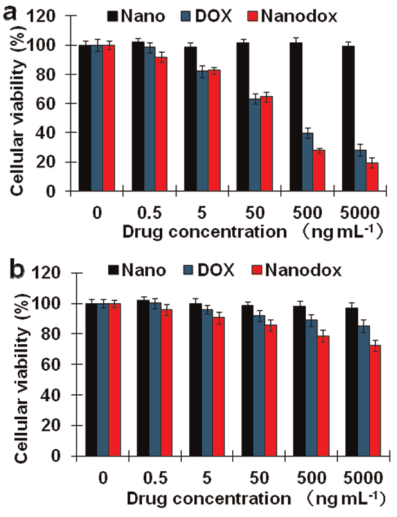

Figure 5. Cell proliferation (MTT) assay. Cell viability assay was carried out to assess the toxicity of the drug to nanoparticles in different ratios in both drug-sensitive and -resistant cells. (a) Drug-sensitive OVACAR8 and (b) drug-resistant OVACR8/ADR cells treated with nanodrug formulation for 48 h. The absorption was measured at 570 nm, and the relative percentage of the control (untreated) cells, which were not exposed to the drug, was used to represent 100% cell viability. Nanodox showed higher toxicity to the cancer cells compared to free drug, and drug-free nanoparticles did not hinder cell growth in both cell types.

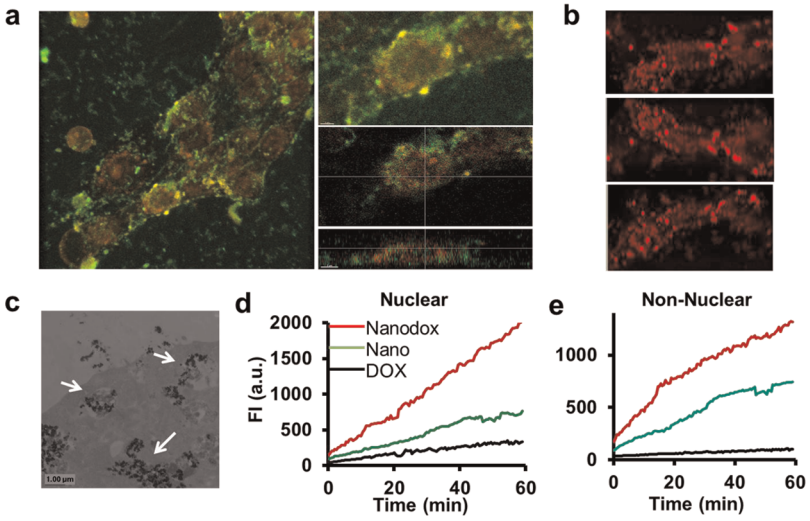

Figure 6. Nuclear mapping of a nanodrug system in a dynamic cellular environment. (a) Live cell snapshots of drug-sensitive cells treated with Nanodox labeled with FITC. Drug DOX is in red; nanoparticles are in green. Nanoparticles mostly remain in the cytoplasm, while the majority of the drug is in the nuclear region. (b) Z-images of Nanodox showing the cellular uptake of DOX. (c) Direct imaging of nanoparticles using TEM. Arrows indicate nanoparticles in the cytoplasm of the cancer cell. (d) Plot showing nuclear and non-nuclear uptake of free DOX, Nanodox, and FITC-labeled SPIONPs (Nano). Uptake pattern is exponential in both the nuclear and non-nuclear regions. DOX loaded on the nanoparticles has the highest rate of reaching the nucleus compared to free DOX.

Observations at longer time intervals showed similar drug uptake patterns in both free DOX and Nanodox formulations for the drug-sensitive cells, whereas uptake of Nanodox was higher than uptake of free drug in drug-resistant cells (Supporting Information Figure S6). These findings were further supported by cell viability assays, where both OVCAR8 and OVCAR8/ADR cells treated with varying drug concentrations in free form and the nanoformulation hindered cell growth with increasing drug concentration (Figure 5). Assays of cell viability of drug-sensitive (Figure 5a) and -resistant (Figure 5b) cancer cells were carried out to check the dosage-dependent killing of the cells using the standard MTT assay. The absorption was measured at 570 nm using a microplate spectrofluorometer, and the relative percentage of the control (untreated) cells, which were not exposed to the drug, was used to represent 100% cell viability.

Mapping of Nanochemo Delivery System in Dynamic Cellular Environment. It is important to determine the fate of the delivery vehicle in addition to the drug, which can be mapped by its intrinsic fluorescence. To achieve this, DOX-loaded nanoparticles were labeled with FITC, and cells were treated and observed live (Figure 6a,b and Supporting Information Video S9). It was found that the drug loaded onto the SPIONPs reached the nuclear region first, whereas the nanoparticles were mostly concentrated in the cytoplasm and plasma membrane. This observation was confirmed by examining the nanoparticles alone without the drug in live microscopy (Supporting Information Video S10) as well as TEM (Figure 6c). Data analysis using the tracking algorithm showed that drug loaded onto the nanoparticles had the highest probability of entering the cell nucleus (Figure 6d). Overall non-nuclear uptake of the drug loaded onto the nanoparticles was higher compared to both free drug and free particles (Figure 6e). The data suggest that the Nanodox formulation could provide an approach to cancer treatment irrespective of the sensitivity of the cells to the drug. Data presented here suggest that computational mapping can lead to prediction of therapeutic results for nuclear-sensitive drugs and drug delivery systems. The masking technique can help elucidate drug uptake, diffusion rate, and transport mechanism. The algorithm can be used for any fluorescent drug, drugs tagged with a fluorescent probe, or a fluorescent probe itself. This *ex vitro* image analysis can also be implemented for *ex vivo* analysis in a dynamic environment.

CONCLUSIONS

In summary, we show that a combination of live cell imaging and tracking can be used to assess variations in nuclear uptake of chemotherapeutics between drug-sensitive and drug-resistant cells. Our results suggest that positively charged magnetic nanoparticles are efficient in carrying chemotherapeutics across cell membranes and that the drug delivered has an increased probability of entering the nucleus. Whereas in sensitive cells free drug and nanoparticle-loaded drug behaved similarly over time, resistant cancer cells appear immune to the free drug. This suggests that a quicker cell-penetrating and drug-releasing nanoparticle formulation acts as a camouflage in counteracting cancer cells resistant to drugs. The data presented here strongly suggest that nuclear mapping of live cells is very important in determining the successful

outcome of a nanoformulation with chemotherapeutics. Moreover, the computational methodology adapted in this study can be used to track specific fluorescent targets of interest in a single cell by masking less relevant regions of cells maintained in a dynamic environment.

METHODS

Synthesis of Nanodox. Nanodox was synthesized following a previously described procedure. Briefly, branched PEI2k (Alfa Aesar) was reacted with 1-iodododecane (Aldrich) in ethanol, and the pure product was obtained as a gummy solid on lyophilization and confirmed by ^{1}H NMR ($CDCl_3$). $Fe(acac)_3$ (2 mmol) was mixed with 1,2-hexadecanediol (10 mmol), oleic acid (6 mmol), and oleylamine (6 mmol) in benzyl ether (20 mL) under nitrogen and heated to reflux (~300 °C) for 1 h. The product was resuspended in hexane in the presence of oleic acid and oleylamine and reprecipitated with ethanol to give SPIONPs. These nanocrystals in hexane were dried under argon and redispersed in chloroform together with alkylated PEI2k and DOX. Then, the mixed solution was slowly added into water with sonication to form Nanodox. The resulting particles were collected by centrifugation and were redispersed in PBS buffer solution. The iron content was analyzed using ICP-MS.[2] For DOX content analysis, a small portion of the product was added to a diluted HCl solution (pH = 5) and incubated for 20 min. The solution was then subjected to fluorescence analysis on a microplate reader (Synergy 2 multi-mode microplate reader, BioTek). The readout at 590 nm was recorded and compared with a standard curve to determine the concentration.

Cell Culture. We thank Dr. Neamati at the University of Southern California for providing the OVCAR8 and OVCAR8/ADR cells. OVCAR8 and OVCAR8/ADR cancer cells were cultured in RPMI (Invitrogen) supplemented with 10% fetal bovine serum at 37 °C in 95% air/5% CO_2. Freshly plated cells were grown overnight, to 50−70% confluency, prior to incubation with nanochemo formulation for live imaging.

FTIR of Nanodrug Formulation. Fourier transform infrared spectroscopy (FTIR) of Nanodox along with controls Alkyl-PEI2k-SPIONPs and DOX alone was done using KBr pellets of each. The wave numbers of the transmittance of each sample were recorded using a PerkinElmer spectrum GX spectrophotometer.

Fluorescence Spectrometry. Fluorescence spectrometer analysis was carried out on DOX-loaded Alkyl-PEI2k-SPIONPs and FITC-conjugated Alkyl-PEI2k-SPIONPs. Fluorescence spectra of Alkyl-PEI2k-SPIONPs-FITC and Alkyl-PEI2k-SPIONPs-DOX nanochemo formulation along with free DOX and FITC alone as controls were obtained using a Perkin-Elmer LS55 fluorescence spectrometer.

Atomic Force Microscope Analysis of Alkyl-PEI2k-IONP. Tapping mode AFM studies were performed on a PicoForce Multimode platform with a Nanoscope V controller (Bruker, Santa Barbara, CA, USA), using a type E scanner head with a FESP-type cantilever, on a mica substrate, and following standard optimizations.

Zeta Potential. To find the surface charge of the nanoparticles, zeta potential analysis was carried out using a Zetasizer Nano series (Zen3600) from Malvern with Zetasizer software 6.0 as the interface.

Confocal Fluorescence Microscopy. DOX-sensitive and -resistant cancer cells were grown into 50−60% confluency on an eight-well chambered LabTek II coverglass, treated with either free drug DOX, Alkyl-PEI2k-SPIONPs-FITC, Nanodox, or DOX loaded and FITC-labeled Alkyl-PEI2k-SPIONPs nanochemo formulation, and live cell time series imaging or Z-stack intercellular uptake analysis was carried out for 1 h. Live cell imaging was performed using an inverted Zeiss LSM 700 confocal microscope equipped with a CO_2 module, heating unit, and heating plate using a 40×/0.75 M27 EC Plan-Neofluar objective. Imaging was carried out at 37 °C in 5% CO_2 with cells plated on a LabTek II coverglass. Images were acquired and processed with the Zeiss Zen 2009 image software. The fluorescence micrographs shown are representative of at least three independent experiments. Average fluorescence intensity was quantified using Zen 2009 software.

Transmission Electron Microscope Imaging of Magnetic Nanocrystals. A specimen of PEI-coated SPIONPs for TEM imaging was obtained by depositing a 3 μL droplet from the aqueous solution onto a Quantifoil grid and leaving it to dry in air. After adsorption for 3 min, the excess solution was blotted with filter paper, washed with a few 3 μL droplets of deionized water in order to remove any dirt, and left to dry. Images were recorded in a Tecnai TF30 TEM (FEI, Hillsboro, OR, USA) equipped with a Gatan Ultrascan 1000 CCD camera (Gatan, Pleasaton, CA, USA).

Cell Proliferation (MTT) assay. Cells were grown to 50−70% confluency overnight in 96-well plates. Next, the medium was aspirated and the cells were incubated with fresh medium containing either free nanoparticles and drug alone or nanochemo formulation for 48 h. Post-treatment, the cells were washed two times with PBS, and cells were incubated for an additional 24 h in fresh medium. MTT was assessed using the CellTiter 96 AQ One Solution cell proliferation assay kit (Promega, WI, USA) and measured optically at 570 nm using a microplate spectrofluorometer.

Conflict of Interest: The authors declare no competing financial interest.

Acknowledgment. This work was supported by the Intramural Research Program (IRP) of the National Institutes of Health (NIH). The work also was partially supported by National Natural Science Foundation of China (81101101, 81028009).

Supporting Information Available: This material is available free of charge *via* the Internet at http://pubs.acs.org.

REFERENCES AND NOTES

1. Zahedi, P.; De Souza, R.; Piquette-Miller, M. Optimizing Cancer Care: Is the Future Bright? *Clin. Pharmacol. Ther.* **2011**, *90*, 347–350.
2. Lameire, N.; Kruse, V.; Rottey, S. Nephrotoxicity of Anticancer Drugs−an Underestimated Problem? *Acta. Clin. Belg.* **2011**, *66*, 337–345.
3. Nielsen, D.; Maare, C.; Skovsgaard, T. Cellular Resistance to Anthracyclines. *Gen. Pharmacol.* **1996**, *27*, 251–255.
4. Pachman, D. R.; Barton, D. L.; Watson, J. C.; Loprinzi, C. L. Chemotherapy-Induced Peripheral Neuropathy: Prevention and Treatment. *Clin. Pharmacol. Ther.* **2011**, *90*, 377–387.
5. Fardell, J. E.; Vardy, J.; Johnston, I. N.; Winocur, G. Chemotherapy and Cognitive Impairment: Treatment Options. *Clin. Pharmacol. Ther.* **2011**, *90*, 366–376.
6. Bergman, P. J. Mechanisms of Anticancer Drug Resistance. *Vet. Clin. North Am. Small Anim. Pract.* **2003**, *33*, 651–667.
7. Weis, S. M.; Cheresh, D. A. Tumor Angiogenesis: Molecular Pathways and Therapeutic Targets. *Nat. Med.* **2011**, *17*, 1359–1370.
8. Davis, M. E.; Chen, Z. G.; Shin, D. M. Nanoparticle Therapeutics: An Emerging Treatment Modality for Cancer. *Nat. Rev. Drug Discovery* **2008**, *7*, 771–782.
9. Bhirde, A. A.; Patel, S.; Sousa, A. A.; Patel, V.; Molinolo, A. A.; Ji, Y.; Leapman, R. D.; Gutkind, J. S.; Rusling, J. F. Distribution and Clearance of PEG-Single-Walled Carbon Nanotube Cancer Drug Delivery Vehicles in Mice. *Nanomedicine (London)* **2010**, *5*, 1535–1546.
10. Yan, Y.; Ochs, C. J.; Such, G. K.; Heath, J. K.; Nice, E. C.; Caruso, F. Bypassing Multidrug Resistance in Cancer Cells with Biodegradable Polymer Capsules. *Adv. Mater.* **2010**, *22*, 5398–5403.

11. Meng, H.; Liong, M.; Xia, T.; Li, Z.; Ji, Z.; Zink, J. I.; Nel, A. E. Engineered Design of Mesoporous Silica Nanoparticles to Deliver Doxorubicin and P-glycoprotein siRNA to Overcome Drug Resistance in a Cancer Cell Line. *ACS Nano* **2010**, *4*, 4539–4550.
12. Sengupta, S.; Eavarone, D.; Capila, I.; Zhao, G.; Watson, N.; Kiziltepe, T.; Sasisekharan, R. Temporal Targeting of Tumour Cells and Neovasculature with a Nanoscale Delivery System. *Nature* **2005**, *436*, 568–572.
13. Ma, X. W.; Zhao, Y. L.; Liang, X. J. Nanodiamond Delivery Circumvents Tumor Resistance to Doxorubicin. *Acta Pharmacol. Sin.* **2011**, *32*, 543–544.
14. Chow, E. K.; Zhang, X. Q.; Chen, M.; Lam, R.; Robinson, E.; Huang, H.; Schaffer, D.; Osawa, E.; Goga, A.; Ho, D. Nanodiamond Therapeutic Delivery Agents Mediate Enhanced Chemoresistant Tumor Treatment. *Sci. Transl. Med.* **2011**, *3*, 73ra21.
15. Bhirde, A. A.; Patel, V.; Gavard, J.; Zhang, G.; Sousa, A. A.; Masedunskas, A.; Leapman, R. D.; Weigert, R.; Gutkind, J. S.; Rusling, J. F. Targeted Killing of Cancer Cells *in Vivo* and *in Vitro* with EGF-Directed Carbon Nanotube-Based Drug Delivery. *ACS Nano* **2009**, *3*, 307–316.
16. Koo, H.; Huh, M. S.; Sun, I. C.; Yuk, S. H.; Choi, K.; Kim, K.; Kwon, I. C. *In Vivo* Targeted Delivery of Nanoparticles for Theranosis. *Acc. Chem. Res.* **2011**, *44*, 1018–1028.
17. Willmann, J. K.; van Bruggen, N.; Dinkelborg, L. M.; Gambhir, S. S. Molecular Imaging in Drug Development. *Nat. Rev. Drug Discovery* **2008**, *7*, 591–607.
18. de Jongh, F. E.; van Veen, R. N.; Veltman, S. J.; de Wit, R.; van der Burg, M. E.; van den Bent, M. J.; Planting, A. S.; Graveland, W. J.; Stoter, G.; Verweij, J. Weekly High-Dose Cisplatin is a Feasible Treatment Option: Analysis on Prognostic Factors for Toxicity in 400 Patients. *Br. J. Cancer* **2003**, *88*, 1199–1206.
19. Fornari, F. A.; Randolph, J. K.; Yalowich, J. C.; Ritke, M. K.; Gewirtz, D. A. Interference by Doxorubicin with DNA Unwinding in MCF-7 Breast Tumor Cells. *Mol. Pharmacol.* **1994**, *45*, 649–656.
20. Momparler, R. L.; Karon, M.; Siegel, S. E.; Avila, F. Effect of Adriamycin on DNA, RNA, and Protein Synthesis in Cell-Free Systems and Intact Cells. *Cancer Res.* **1976**, *36*, 2891–2895.
21. Zeller, C.; Dai, W.; Steele, N. L.; Siddiq, A.; Walley, A. J.; Wilhelm-Benartzi, C. S.; Rizzo, S.; van der Zee, A.; Plumb, J. A.; Brown, R. Candidate DNA Methylation Drivers of Acquired Cisplatin Resistance in Ovarian Cancer Identified by Methylome and Expression Profiling. *Oncogene* **2012**, Jan 16. doi: 10.1038/onc.2011.611.
22. Torchilin, V. P. Fluorescence Microscopy to Follow the Targeting of Liposomes and Micelles to Cells and Their Intracellular Fate. *Adv. Drug Delivery Rev.* **2005**, *57*, 95–109.
23. Hamilton, N. Quantification and Its Applications in Fluorescent Microscopy Imaging. *Traffic* **2009**, *10*, 951–961.
24. Muzzey, D.; van Oudenaarden, A. Quantitative Time-Lapse Fluorescence Microscopy in Single Cells. *Annu. Rev. Cell Dev. Biol.* **2009**, *25*, 301–327.
25. Mikhaylov, G.; Mikac, U.; Magaeva, A. A.; Itin, V. I.; Naiden, E. P.; Psakhye, I.; Babes, L.; Reinheckel, T.; Peters, C.; Zeiser, R.; Bogyo, M.; Turk, V.; Psakhye, S. G.; Turk, B.; Vasiljeva, O. Ferri-Liposomes as an MRI-Visible Drug-Delivery System for Targeting Tumours and Their Microenvironment. *Nat. Nanotechnol.* **2011**, *6*, 594–602.
26. Namiki, Y.; Namiki, T.; Yoshida, H.; Ishii, Y.; Tsubota, A.; Koido, S.; Nariai, K.; Mitsunaga, M.; Yanagisawa, S.; Kashiwagi, H.; Mabashi, Y.; Yumoto, Y.; Hoshina, S.; Fujise, K.; Tada, N. A Novel Magnetic Crystal-Lipid Nanostructure for Magnetically Guided *in Vivo* Gene Delivery. *Nat. Nanotechnol.* **2009**, *4*, 598–606.
27. Plank, C. Nanomedicine: Silence the Target. *Nat. Nanotechnol.* **2009**, *4*, 544–545.
28. Paoloni, M.; Khanna, C. Translation of New Cancer Treatments from Pet Dogs to Humans. *Nat. Rev. Cancer* **2008**, *8*, 147–156.
29. Otterson, G. A.; Villalona-Calero, M. A.; Sharma, S.; Kris, M. G.; Imondi, A.; Gerber, M.; White, D. A.; Ratain, M. J.; Schiller, J. H.; Sandler, A.; Kraut, M.; Mani, S.; Murren, J. R. Phase I Study of Inhaled Doxorubicin for Patients with Metastatic Tumors to the Lungs. *Clin. Cancer Res.* **2007**, *13*, 1246–1252.
30. Bhirde, A.; Guo, N.; Chen, X. Targeted Nanoprobes Reveal Early Time Point Kinetics *in Vivo* by Time-Resolved MRI. *Theranostics* **2011**, *1*, 274–276.
31. Weinstein, J. S.; Varallyay, C. G.; Dosa, E.; Gahramanov, S.; Hamilton, B.; Rooney, W. D.; Muldoon, L. L.; Neuwelt, E. A. Superparamagnetic Iron Oxide Nanoparticles: Diagnostic Magnetic Resonance Imaging and Potential Therapeutic Applications in Neurooncology and Central Nervous System Inflammatory Pathologies, a Review. *J. Cereb. Blood Flow Metab.* **2010**, *30*, 15–35.
32. Xie, J.; Jon, S. Magnetic Nanoparticle-Based Theranostics. *Theranostics* **2012**, *2*, 122–124.
33. Quan, Q.; Xie, J.; Gao, H.; Yang, M.; Zhang, F.; Liu, G.; Lin, X.; Wang, A.; Eden, H. S.; Lee, S.; Zhang, G.; Chen, X. HSA Coated Iron Oxide Nanoparticles as Drug Delivery Vehicles for Cancer Therapy. *Mol. Pharm.* **2011**, *8*, 1669–1676.
34. Brule, S.; Levy, M.; Wilhelm, C.; Letourneur, D.; Gazeau, F.; Menager, C.; Le Visage, C. Doxorubicin Release Triggered by Alginate Embedded Magnetic Nanoheaters: a Combined Therapy. *Adv. Mater.* **2011**, *23*, 787–790.
35. Kievit, F. M.; Wang, F. Y.; Fang, C.; Mok, H.; Wang, K.; Silber, J. R.; Ellenbogen, R. G.; Zhang, M. Doxorubicin Loaded Iron Oxide Nanoparticles Overcome Multidrug Resistance in Cancer *in Vitro*. *J. Controlled Release* **2011**, *152*, 76–83.
36. Duwez, A. S.; Cuenot, S.; Jerome, C.; Gabriel, S.; Jerome, R.; Rapino, S.; Zerbetto, F. Mechanochemistry: Targeted Delivery of Single Molecules. *Nat. Nanotechnol.* **2006**, *1*, 122–125.